Under-Displaced Normal Faults: Strain Accommodation along an Early-Stage Rift-Bounding Fault in the Southern Malawi Rift

Oyewande O. Ojo[1], Leonard O. Ohenhen[2], Folarin Kolawole[3,4], Steven G. Johnson[1], Patrick R. Chindandali[5], Estella A. Atekwana[6], and Daniel A. Laó-Dávila[1]

[1]Boone Pickens School of Geology, Oklahoma State University, 105 Noble Research Center, Stillwater, OK 74078-3031, USA
[2]Department of Geosciences, Virginia Tech, Blacksburg, VA, USA.
[3]BP America, 501 West Lake Blvd., Houston, TX 77079, USA
[4]Lamont-Doherty Earth Observatory, Columbia University, 61 Rte 9W, Palisades, NY 10964, USA
[5]Geological Survey Department, P.O. Box 27, Zomba, Malawi
[6]Department of Earth and Planetary Sciences, University of California, Davis, One Shields Avenue, Davis, CA 95616, USA

Corresponding author: Oyewande Ojo (oyewande.ojo@okstate.edu)

Abstract

One of the fundamental problems in continental rift segmentation and propagation is how strain is accommodated along large rift-bounding faults (border faults) since the segmentation of propagating border faults control the expression of rift zones, syn-rift depo-centers, and long-term basin evolution. In the southern Malawi Rift, where previous studies on the early-stage rifting only assessed border fault structure from surficial and topographic expression, we integrate surface and subsurface data to investigate border fault segmentation, linkage, and growth as proxies for strain accommodation along the Bilila-Mtakataka Fault (BMF) System. We used 30 m-resolution topographic relief maps, electrical resistivity tomography (ERT), and high-resolution aeromagnetic data to characterize the detailed fault geometry and provide a more robust estimate of along-fault displacement distribution. Our results reveal a discrepancy between sub-aerial segmentation of the BMF geometry (6 segments), scarp height (5 segments) reflecting the most recent fault offset, and cumulative throw (3 segments) reflecting the long-term fault offset. We also observe that although the BMF exhibits continuity of sub-aerial scarps along its length, the throw distribution shows a higher estimate at the Northern-to-Central segment relay zone (423 m absolute, 364 m moving median) compared to the Central-to-Southern segment relay zone (371 m absolute, 297 m moving median). The ERT profiles across the relay zones suggest a shallower basement and a possible canyon-mouth alluvial fan stratigraphy at the Central-to-Southern segment relay zone, which contrasts the deeper basement and 'simpler' electrical stratigraphy at the Northern-to-Central relay. The results suggest a more complex long-term evolution of the BMF than was assumed in previous studies. A comparison of maximum throw-length estimates of the BMF with those of other well-studied Malawi Rift border faults and global normal fault populations suggest that although the BMF has possibly reached its maximum length, just as the other border faults, it remains

largely under-displaced. We suggest that the BMF may continue to accrue significant strain as tectonic extension progresses in southern Malawi Rift, thus posing a major seismic hazard in the region.

1.0 Introduction

During continental rifting, normal faults grow by strain accommodation leading the progressive evolution of their associated rift basins (Muirhead et al., 2019; Nixon et al., 2016; Calais et al., 2008). Strain accommodation, strain transfer, and deformational styles in early-stage continental rifts are often influenced by regional tectonics stress orientation, lateral variation in crustal stretching rates, pre-existing basement structures, and lithosphere rheology (Rotevatn et al., 2019, Peacock et al., 2017, Nixon et al., 2016; Muirhead et al., 2019; Wright et al., 2020; Gouiza & Naliboff, 2021; Kolawole et al., 2021a). During continental extension, strain is accommodated by crustal deformation in the form of rift faulting, and their distribution can be quantified from a series of structural and tectonic attributes associated with fault growth (Bonini et al., 2005). These attributes include the younging direction of the border faults (Abbate and Sagri, 1980; WoldeGabriel et al., 1990, 2016), the changes in border fault length and the elastic thickness of the lithosphere (Hayward and Ebinger, 1996), lateral variation in ages of syn-rift deposits (Furman et al., 2004; Maguire et al., 2003), and lateral migration of magmatic activity (Zanettin et al., 1980).

Large normal faults typically develop by an initial nucleation of isolated segments which progressively propagate and link up with one another. The interaction and linkage of adjacent propagating fault segments typically occur at structurally complex areas, referred to as 'strain transfer zones' or 'relay zones' (e.g., Morley et al. 1990; Morley, 1999; Jackson and Rotevatn, 2013; Childs et al., 2017). These relay zones accommodate the along- and across-axis variations in the magnitude of subsidence of grabens and the elevation of uplifted rift flanks or normal fault footwall blocks (Rosendahl, 1987; Morley et al., 1990; Faulds and Varga, 1998; Morley, 1999).

There exists an empirical relationship between fault length and displacement, which provides insight into the mechanics of fault growth, and presents a useful tool for characterizing the extent and rates of tectonic deformation in continental rift zones (Bergen and Shaw, 2010). Scaling laws of maximum displacement versus fault length exhibit a power-law relationship (e.g., Walsh and Watterson, 1988; Peacock and Sanderson, 1991; Cowie and Scholz, 1992b; Dawers et al., 1993; Manighetti et al., 2001). Normal fault propagation models suggest that faults grow along fault tips, and that there is a proportional increase in the length of the fault and maximum displacement throughout the slip history of the fault ('propagating fault model', e.g., Walsh and Watterson, 1988; Dawers et al., 1993; Cartwright et al., 1995; Walsh et al., 2003). Another model ('constant-length model') suggest that the total length of the fault is attained early in the fault history and that most displacement is accumulated after the total length has been established (Walsh et al., 2003; Nicol et al., 2005; Densmore et al., 2007; Schlagenhauf et al., 2008; Jackson and Rotevatn, 2013; Nixon et al., 2016).

Rotevatn et al. (2019) proposed a hybrid fault growth model which suggests that normal faults initially grow by lateral propagation in the early stages of the fault lifespan (20-30 % of the fault lifespan) to establish the total length of the fault, then, subsequently grow by constant-length model for the rest of the fault lifespan (70-80 % of the fault lifespan). Also, recent numerical models by Pan et al. (2020) revealed that normal fault arrays evolve via alternating phases of fault-lengthening and localization. However, the process of strain accommodation by normal fault growth during the early stages of continental extension remains less understood. Since the segments of important rift faults are often established during early-stage rifting, this knowledge-gap limits the complete understanding of the processes that govern the variation of structural architecture along margins of continental break-up. In rift basins, upper crustal extension is accommodated by two groups of fault systems: border faults and intra-rift faults (e.g., Corti, 2009). The border faults are the largest faults bounding a rift segment and often accommodate the most offset, whereas intra-rift faults are the smaller faults that are found within the inner depressions of rift basins (Scholz & Contreras, 1998; Goldsworthy & Jackson, 2001; Ebinger, 2005; Corti, 2009; Muirhead et al., 2019). However, the new SEGMeNT data over lake Malawi show some very long intra rift faults with large throws of several km (Shillington et al., 2020).

In this contribution, we investigate the detailed structure and distribution of displacement along the Bilila-Mtakataka Fault (BMF), an active border fault in the southern Malawi Rift, East Africa (Figures 1a-c), to understand the pattern of fault growth and strain accommodation in areas of early-stage continental extension. This fault is suggested to be seismogenic and may have hosted the M 6.2, 9 km NNW of Salima, Malawi at a depth of about 30.3km (from USGS earthquake hazard program). In addition, the results of the study provide insight into the seismic hazard of large rift-bounding normal faults.

2.0 Geologic and Tectonic Setting of the Malawi Rift

Eastern Africa has witnessed three phases of tectonic extension during the Phanerozoic, among which the East African Rift System (EARS) represents the third and currently active phase of extension which began in the Oligocene (Delvaux, 1991; Roberts et al., 2012). The ~750 km-long N-S trending Malawi rift represents a prominent segment of the EARS (Ebinger, 1989; Ebinger et al., 1987), and is located near the southern tip of the magma-poor western branch of the rift system (Figures 1a-b). The Malawi Rift is sub-divided into eight distinct 100 – 150 km-long grabens and half grabens which exhibit alternating polarities along-strike (Laó-Dávila et al., 2015). To the north, the northernmost graben, the 'Karonga' or North Basin terminates at the Rungwe Volcanic Province, whereas, the southernmost graben of the Malawi Rift is defined by the Zomba Graben which terminates at a zone of exposed basement extending into the Shire Rift Zone (Kolawole et al., 2021b).

Although the Malawi Rift largely developed during the Cenozoic evolution of the EARS, it is proposed to have propagated southwards based on: (1) the

extensive outcrops of Mesozoic syn-rift sequences in the northern basins of the rift which are absent in the south (Delvaux, 2001; Dunlaya, 2017; Wedmore et al., 2020), (2) southward thinning of the syn-rift sedimentary cover (Flannery & Rosendahl, 1990; Specht & Rosendahl, 1989), and (3) southward decrease in the throw of border faults with corresponding changes in the seismic depositional facies of the syn-rift sequences (Scholz et al., 2020). However, it is also plausible that the initiation of Cenozoic rifting across the entire length of the Malawi Rift could have been synchronous and that rifting occurs at different rates along the rift length (Ojo et al., 2021). Overall, crustal stretching rates decrease from north (4.5 mm yr^{-1}) to south 1.3 mm yr^{-1} (Stamps et al., 2008; 2018; 2021). The major grabens and some associated major border faults in the southern Malawi Rift are the Makanjira Graben (Bilila-Mtakataka and Malombe faults), and the Zomba Graben (Zomba and Lisungwe faults).

2.1. The Bilila-Mtakataka Fault (BMF)

The Bilila-Mtakataka fault (BMF) is one of the most prominent rift-bounding faults in southern Malawi Rift, characterized by a steep, clean fault scarp of about 4-15 m height, and was first highlighted in Walshaw (1965) and Dawson and Kirkpatrick (1968) based on its excellent topographic expression in topographic relief maps (Figs. 2a-e) and in the field (Figs. 2f-g). Although the fault has been estimated to be an outstanding >100 km-long continuous normal fault scarp (Jackson et al., 1997; Hodges et al., 2018), the subsurface structure of the fault remains unknown. Based on the large length of the BMF, Jackson et al. (1997) proposed the possible control of a thick seismogenic layer on the fault evolution. The BMF is suggested to have developed within a strong lithosphere with an effective elastic thickness of about 30 km (Jackson and Blenkinsop, 1993).

The surficial geomorphology of the BMF comprises a basal metamorphic basement that is composed of a shallower fractured and weathered basement. It is also made up of a deeper fresh basement, above which the syn-rift sediments accumulate in the hanging wall of the BMF. The sediments are primarily alluvial sediments with colluvial lobes confined to the foot of the fault escarpment(Walshaw, 1965). The sedimentary basin in the hanging wall is a fluvio-lacustrine depositional environment with occasional sediment inundation from 100 yr-cycles of over-flooding events in Lake Malawi (Dulanya, 2017; Dulanya et al., 2014). This is due to the several transverse cutting streams that originate from the from the elevated footwall areas (e.g., Nsipe-Livelezi Shelf watershed) and flow downslope, across the BMF escarpment into the basin where they either empty into Lake Malawi or join the Bwanje River which is the prominent axial stream draining the Makanjira Sub-basin (Fig. 2d). The northward-flowing Bwanje River originates from a watershed in an elevated area near Balaka that marks the southern tip of the BMF, separating the Bwanje valley in the Makajinra Trough from the Liwawadzi Valley in Zomba Graben to the south (Walshaw, 1965).

Hodges et al., (2018) investigated the fault geometry of the BMF and controls

on the rift by using high-resolution satellite and field measurements to highlight the geometry of the BMF and the corresponding foliations in the crystalline basement footwall rocks. The BMF was suggested to have scarp height that is likely influenced by the near-surface fault geometry. This conclusion is inferred and indicated by where the locally well oriented metamorphic foliations are reactivated in preference over growth of new faults (Hodges et al., 2018).

3.0 Methodology

In this study, we integrate topographic analysis with geophysical imaging of the subsurface structure along the Bilila-Mtakataka Fault (BMF). We obtain along-fault scarp height and footwall height measurements from Shuttle Radar Topography Mission (SRTM) elevation data. Scarp height provides the sub-aerial component of recent fault displacement and footwall height provides a measure of sub-aerial component of long-term cumulative fault displacement. We utilize aeromagnetic transform techniques to generate a depth-to-magnetic basement map which provides estimates of the subsurface component of long-term cumulative fault displacement. Our sampling points from both the SRTM topographic data and aeromagnetic depth-to-basement are approximately the same along the entire trace length of the fault. At each sample point, the estimated throw represents its relative value across a fault surface i.e., relative to depth, or its maximum value (Tao and Alves, 2019). We utilize Electrical Resistivity Tomography (ERT) to investigate the fault zone and assess the lateral variation of local hanging wall stratigraphic architecture along-trend of the fault.

3.1 Scarp and Footwall Height Measurements from Digital Elevation Models

The fault scarp indicates the most recent slip along a normal fault. The scarp heights were extracted and measured from a 30-m resolution Shuttle Radar Topography Mission (SRTM)-Digital Elevation Model (DEM). Fault scarps were outlined and traced from a hillshade map created on QGIS using the SRTM-DEM. Elevation profiles were taken perpendicularly across the fault at every 1 km because the sampling interval/fault length ratio ( ) has to be <0.05 for adequate resolution and to avoid loss of vital information. The $= 0.05$ threshold value is recommended for faults of any scale and profiles should be taken at intervals that are <5% of the total length of fault if they are believed to be segmented (Tao and Alves, 2019). The scarp height (h) is the vertical distance of the steepest slope along the local footwall elevation. The vertical distance of the local footwall slope is the local footwall elevation i.e. the top of the local footwall slope to the top of the local hanging wall that hosts the fault scarp (h'; Caskey, 1995; Wedmore et al., 2019; Hornsby et al., 2020). We measured the vertical distance of the footwall between the steepest points along the fault scarps (as shown in Fig. 3).The scarp heights and local footwall heights were measured and plotted against fault length to produce a displacement-length relationship. The methodology adopted in this study accounts for variables such as ancient topography, weathering and erosion, and structural irregularities

due to the subjective nature of this process and observed irregularities along the fault trace. Our measurements are likely to be underestimated as the escarpment continues up to a higher elevation, however since it is difficult to constrain the component of paleotopography in the footwall elevation, we take a conservative approach.

We note that the method of scarp height measurement adopted in this study is different from the methodology used by Hodges et al., (2018) which adopted a semi-automated approach to extracting and measuring the scarp height. Their study measured the 'vertical separation' as an estimate of fault throw rather than scarp height. We also extended the BMF fault trace further to the north than what other studies have studied and focused on investigating the evolution of normal border faults in that part of the rift. Segments on the scarp height plot along the fault length were classified as part of the fault between two consecutive minima separated by the maximum point between them. Transfer zones on the scarp height plot are classified as flat parts of the fault between two consecutive minima and not separated by any maximum points.

3.2 Estimation of Depth-to-Magnetic Basement from Aeromagnetic Data

To assess the along-fault distribution of subsurface components of fault throw, we estimated the depth to the top of the magnetic basement (d) in the hanging wall of the BMF using high resolution aeromagnetic data from Malawi. Since the primary and dominant magnetic source in the study area is the crystalline basement, d is taken to be a measure of the depth to the crystalline basement. For our basement depth calculation, we use the Source Parameter Imaging (SPI) transform of the total magnetic intensity (TMI) anomaly grid (Blakely and Simpson, 1986; Thurston and Smith, 1997; Smith et al., 1998).

The SPI formulation assumes a step-type source in which the depth to the top of the magnetic source is an inverse of the peak value of the local wavenumber over the step source.

SPI Depth = $1/K_{max}$ (1)

$K = \sqrt{(}$ [dT/dx]^2 + [dT/dy]^2) (2)

T = $\tan^{-1}$ (VDR/THDR) (3)

VDR = dM/dz (4)

THDR = $\sqrt{(}$ [dM/dx]^2 + [dM/dy]^2) (5)

where K_{max} is the peak value of the local wavenumber K over the step source, T is the Tilt derivative, VDR is the first vertical derivative, THDR is the total horizontal derivative, and M is the total magnetic field anomaly (TMI).

The computation of the SPI depth solutions across a TMI grid involves an initial computation of the local wavenumber from the tilt derivative, then smoothening of the wavenumber grid using a Hanning filter to reduce noise, and finally,

localized peak wavenumber detection using a Blakely test (Blakely and Simpson, 1986). Finally, we extracted the values of depth-to-magnetic basement in the hanging wall at a distance of 1 km basinward from the base of the fault scarp at each scarp height sample point (Fig. 3). We use the 1 km depth extraction distance for consistency, since the deepest sections near the BMF segment centers and shallowest sections in the relay zones commonly occur within this distance from the base-scarp. The estimation of depth-to-magnetic basement from aeromagnetic data has an inferred accuracy of ±20% (Gay, 2009). Thus, we indicate an error bar of ±20% of the measurements in the depth-to-basement scatter plot.

Fault throw can be estimated by the minimum cumulative vertical component of fault displacement between correlative footwall and hanging-wall (Muirhead et al., 2016; Tao and Alves, 2019) using surface and sub-surface components of the rift border fault. Thus, to obtain the minimum throw (T) at each sample point along the BMF, we use:

$$T = h' + d \quad (6)$$

where, h' is the measured local footwall height, and d is the depth-to-magnetic basement. Along-fault throw-distance plots present a view of fault segmentation which then provide insights into the complex structural evolution of the BMF in terms of its linkage and long-term growth.

3.3 Electrical Resistivity Tomography (ERT) of Fault Zone and Local Hanging Wall Stratigraphic Architecture

The BMF is composed of multiple segments as defined by surface scarp height variation and plan-view geometry (this study and Hodge et al., 2018). To characterize the local subsurface electrical structure in the hanging wall of the BMF, we acquired four 2-D electrical resistivity profiles across the segments and their relay zones (Fig. 2a). Two of the survey profiles were acquired near the central part of two of the fault segments (ERT Profiles 1 and 4), and the other two profiles were acquired near two of the relay zones (ERT Profiles 2 and 3). The survey transects are oriented perpendicular to the fault trend, extending across the BMF fault scarp at each of the survey locations, except for a section along ERT Profile 3 which is slightly oblique to the fault trend due to land accessibility challenges on the field (Figs. 2c-e). Along ERT Profile 3, the fault-oblique section occurs across the fault scarp, whereas, the southwestern and northeastern sections of the profile are at higher angles to the fault trend (Fig. 2d). At all the survey locations, the profiles extend from the footwall of the fault, across the top and base scarps, and terminate at considerable distance into the hanging wall (Figs. 2f-g).

We utilized a 10 channel Iris Syscal Pro resistivity meter with 72 electrodes and a 10 m electrode spacing along the four profiles (Fig. 2h-i). Due to field constraints, three of the profiles (ERT Profiles 1, 2, and 4) were each 710 m-long, and the fourth (ERT Profile 3) was 1070 m-long (acquired using roll-along sequence). Based on the ERT profile lengths, we consider that the surveys only

image the fault zone and electrical stratigraphy of the local hanging wall slope of the fault. Except for ERT Profile 1 at which only the dipole-dipole array was acquired, we acquired both Wenner-Schlumberger and dipole-dipole arrays for all the profiles. The Wenner-Schlumberger array is sensitive to both horizontal and vertical structures, while the dipole-dipole array is good for mapping vertical structures (Loke, 2002).

To obtain a dense dataset with good lateral and vertical resolution, we combined the data from both array types to create a mixed array using Prosys II (Zhou, et al., 2002). Bad data points were culled using the RMS statistics based on preliminary inversion, and the final inversion model results have RMS error <10%. Supporting Information Table S1 contains the relevant details of the inversion parameters applied. The data processing and inversion were performed using RES2DINV software (Loke & Barker, 1996) using the smoothness-constrained least-squares method (Claerbout and Muir 1973; deGroot-Hedlin and Constable 1990). The least squares formulation provides a RMS (root-mean-squared) value which is the factor of discrepancy that describes the differences between the logarithms of the measured and calculated apparent resistivity values, such that the RMS error value of a model inversion is the measure of data fit for the inversion. The parameterization of the inversion carried out in our study is provided in supplementary table S1 of the supplementary document. We present the results of the 2-D resistivity tomography along with plots of model sensitivity and uncertainty estimates.

The model sensitivity is a measure of the reliability of the inversion model (Loke, 2002). The higher the sensitivity value, the more reliable the model resistivity value and vice-versa (Loke, 2002). We defined low (less than 0.1), medium (values between 0.1 and 2.0), and high (greater than 2.0) sensitivity values for each inversion model (supplementary information figures S1 & S2) and used the region of low sensitivity (shown as shaded polygons in the inverse model cross-sections) to constrain the interpretation of the resistivity sections.

Although there is no borehole data available in the study area to provide a strong constraint on the inversion profile interpretations, we adopt an 'in-context' approach for interpretation, which relies on the tectonic setting of the target structure (NE-dipping active normal fault; Fig. 2a), the surface locations of exposed crystalline basement and sedimentary cover along the survey profiles (Fig. 2b), and the depositional environment of the basin (fluvio-lacustrine setting; Dulanya, 2014; 2017). The typical resistivity values for crystalline basement have a range of 1000 - 100000 ohm-m, and those of unconsolidated sedimentary deposits and weathered basement racks range 2 - 1000 ohm-m (Palacky, 1987; Minsley et al., 2010).

4.0 Results

4.1 Along-Fault Distribution of Scarp Height (h) and Local Footwall Height (h')

At the surface, the NW-trending BMF trace is approximately 152 km in length

and exhibits plan-view geometrical (Fig. 2a) and scarp segmentation (Fig. 4). Based on the along-fault distribution of scarp height and local footwall height, the profiles (Fig. 4) show that the border fault is subdivided into five scarp segments (Scarp Segments 1-5). Scarp Segment 1 is the northernmost segment along the BMF and it is 57 km long and has a maximum scarp height of 31 m, which clearly contrasts the plan-view geometrical segmentation of this section of the fault (Ngodzi and Mtakataka geometrical segments). Scarp Segment 2 is 20 km in length with a maximum scarp of 25 m. Scarp Segment 3 has a length of 17 km and maximum scarp height of 33 m, to the south of which is Scarp Segment 4 which is 15 km long with 20 m of scarp height. Scarp Segment 5 is the southernmost segment along the BMF and it has a length of 43 km with scarp height of about 15m.

Scarp Segment 1 is the northernmost segment along the BMF and it is 57 km long and has a max. local footwall height of 61 m, which clearly contrasts the plan-view geometrical segmentation of this section of the fault (Ngodzi and Mtakataka geometrical segments). Scarp Segment 2 is 20 km in length with a max. local footwall height of 56 m. Scarp Segment 3 has a length of 17 km and max. local footwall height of 86 m, to the south of which is Scarp Segment 4 which is 15 km long with 72 m of max. local footwall height. Scarp Segment 5 is the southernmost segment along the BMF and it has a length of 43 km with max. local footwall height of about 65m.

We note that the relay zone (zone of transition between segments) between Scarp Segments 4 and 5 shows the greatest magnitude of scarp height minima compared to the other relay zones. Also, we note that in both plan-view geometry (Fig. 2) and scarp height distribution (Fig. 4), the longest 'continuous' segments along the BMF are the northern-most segment (Scarp Segment 1) and the southernmost segment (Scarp Segment 5). In between these two long segments, three smaller segments (Scarp Segment 2, 3 & 4) are found.

Overall, the broad trends illustrated by the moving median curves suggest that these five sub-aerial segments can be grouped into three large composite segments considering the relative magnitudes of scarp height minima along the profile. These composite segments consist of a northern composite segment (includes Ngodzi and Mtakataka geometrical segments), a central composite segment (Mua, Kasinje, and Chitsulo geometrical segments), and a southern composite segment (Bilila geometrical segment). The scarp height and local footwall height plots show similar but higher magnitudes in both the northern and central composite segments and appear to gently decrease towards the southern end of the border fault system. Whereas, the maximum local footwall height shows the highest values in the central composite segment and somewhat similar magnitudes in the northern and southern composite segments..

4.2 Along-Fault Distribution of Depth-to-Basement

The calculation of depth-to-magnetic basement from the total magnetic intensity aeromagnetic grid (Fig. 5a) using the SPI method produced a grid map of the

depth solutions (Fig. 5b). In general, the SPI map shows <500 m basement depths in which the basement deepens westward towards the BMF escarpment and shallows eastward towards the Shire Horst to the southeast and Lake Malawi to the northeast (Fig. 5b). The shallowing of the basement is most pronounced in the southeast, along the Chitsulo and Bilila segments where the width of sediment cover in the BMF hanging wall is narrow (<7 km-wide) compared to 8 - 28 km-wide regions further north along the Mtakataka-to-Kasinje segments. We note the presence of a prominent narrow region of shallow basement (~120 m) that extends southwest from the Shire Horst into the relay zone between the Kasinje and Chitsula segments of the BMF (Fig. 5c). In comparison to the other relay zones along the BMF, this relay zone exhibits the shallowest basement. In addition, the narrow region of shallow basement marks the transition from the southern BMF hanging wall region with narrow sedimentary cover to the northern BMF hanging wall region with wider sedimentary cover (Fig. 5c).

Along the BMF, the extracted basement depth values show a distribution that roughly mimics the general trend of the maximum local footwall height (Fig. 6). The values are highest near the center but decrease to ~180 m near the northern fault tip and ~100 m near the southern tip. We observe two prominent minima along the moving median curve: one at distance ~42 m, and the other at distance 100 m, thus delineating three large segments which are consistent with the composite segments of the scarp height fitting curve (. We refer to these large segments as the Northern Segment (extending between distance 0 - 40 m), Central Segment (distance 45 - 100 m), and the Southern Segment (distance 105 - 150 m). The basement attains a maximum depth of ~460 m in the Northern Segment. ~500 m in the Central Segment, and ~460 m in the Southern Segment (Fig. 10).

4.3 Along-Fault Distribution of Cumulative Throw, T

We estimated the minimum cumulative throw, T, at each sampling point to produce a distance-throw plot along the BMF by adding the maximum local footwall height and SPI depth-to-basement results (Fig. 6). The fitting curve of the moving median of minimum cumulative throw shows a similar trend as those of both the depth-to-basement and maximum local footwall height, consistent with the delineation of three large segments along the BMF (Fig. 6). Overall, the maximum Talong the fault is ~560 m, located near the center of the entire fault system. The minimum T estimates are ~120 m at the southern tip of the fault and ~190 m near the northern fault tip. However, the Northern Composite Segment shows a maximum T of ~500 m, the Central Composite Segment ~560 m, and the Southern Composite Segment ~480 m.

4.4 Subsurface Electrical Resistivity Structure

In general, the ERT Profiles 1 to 4 (Figs. 7-10) commonly show three geoelectrical layers that are truncated and offset by sub-vertical discontinuities. On each profile, the most prominent among the sub-vertical discontinuities is colocated with the base of the BMF escarpment at the surface. ERT Profile 1, acquired

near the center of Scarp Segment 1 (Ngodzi) in the north-western section of the BMF (Fig. 2c) and shows three geoelectric layers (Fig. 7). The topmost layer is a ~10 m thick laterally-continuous layer dominated by moderate resistivity values (~10 - 100 ohm-m). This layer overlies a 120 m-thick layer that is composed of generally low resistivity zones (<100 ohm-m). The third and basal geoelectric layer is a very high-resistivity layer (> 1000 ohm-m) that extends up to the near-surface in the northwestern part of all the profiles where it is confined to the footwall of the BMF escarpment.

ERT Profile 2 (Fig. 8) was acquired near the zone of segmentation (relay zone) between Scarp Segments 1 and 2 (transition from Mtakataka to Mua geometrical segments) in the northwestern section of the BMF (Fig. 2c). The inversion model shows three geoelectrical layers with a 20 - 40 m-thick topmost layer that is dominated by ~10 - 300 ohm-m resistivity anomalies, which appear to mimic the electrical character of the topmost layer in ERT Profile line 1. This topmost layer is underlain by a ~100 m-thick low-resistivity (<10 ohm-m) layer which is underlain by a basal layer of elevated resistivity values (>30 ohm m). Similar to ERT Profile 1, the footwall of the BMF scarp is dominated by high-resistivity anomalies (> 1000 ohm-m).

ERT Profile 3 (Fig. 9) was acquired at the relay zone in-between Scarp Segments 3 and 4 (transition from Kasinje to Citsulo geometrical segments) in the central section of the BMF (Fig. 2). The inversion result of this profile contrasts with the other ERT profiles in that it shows a complex geoelectrical model in which the top of the basal high-resistivity layer defines a dipping (not sub-vertical) slope that is colocated with the base of the BMF scarp. The basal geoelectric layer is overlain by a layer that consists of mixed geoelectric bodies in which a possible shallower unit is characterized by 10 - 60 ohm m resistivity values and has a thickness of 20 - 40 m which thickens to >70 m basinward (near the far eastern end of the profile); and a deeper layer is defined by discrete bodies of moderate-resistivity bodies (60- 300 ohm m) hosted within a ~60 ohm m background resistivity anomaly. ERT Profile 4 (Fig. 10), acquired near the center of the Scarp Segment 5 (Bilila geometrical segment) in the southernmost section of the BMF, is generally characterized by low-resistivity zones (<30 ohm m) in the hanging wall of the BMF scarp and very high-resistivity zones in the footwall of the scarp. The BMF scarp is colocated with a strongly subvertical discontinuity that extends across the inversion model.

The inversion results for ERT Profiles 1 and 2 shows 75 ° dip angle for the BMF electrical gradient (Figs.7 - 8), but 70 ° on ERT Profile 4 (Fig. 10). These are useful estimates of subsurface dip of the BMF considering that the profiles are orthogonal to the fault trend. The relative sensitivity of the inverse models are mostly composed of model blocks of medium and high sensitivities, particularly within the upper 40 m interval (Supporting Information S1). Also, the regions with high resistivity values compared to the surrounding regions generally show low sensitivities (Supporting Information S1).

5.0 Discussion

5.1 Integration of Topographic and Subsurface Observations Along the Bilila-Mtakataka Fault Zone

The results of this study reveal a distinct difference in the segmentation pattern observable along the surface trace of the BMF (i.e. scarp and geometrical segmentation; Fig. 4) and the segmentation pattern shown by the along-fault distribution of depth-to-basement(Fig. 6). The geometrical segmentation shows six segments (Fig. 4; Hodges et al., 2018) and scarp segmentation shows five segments (Fig. 4), whereas the depth-to-basement and overall cumulative throw segmentation show three segments (Fig. 6). Since the cumulative throw is most representative of the long-term displacement pattern along a fault, we posit that the subsurface component of displacement should be ignored in the investigation of fault zone structure and segmentation as it can contrast observations at the surface. However, although *h'* is also part of the subaerial component of fault displacement (Fig. 3), the similarity of its segmentation pattern with the depth-to-basement (Fig. 6) suggest that the *h'* may preserve information on the long-term displacement pattern along a fault. In addition, we emphasize that along-fault variation of scarp height (scarp segmentation) and geometrical segmentation are associated with the more recent rupture displacement patterns along a fault and may not be necessarily representative of the distribution of long-term cumulative displacement and segmentation of a fault. In essence, our results suggest that the geometrical complexity observed along a surface fault trace might not always be present at depth.

At the scale of the Makanjira Sub-basin (i.e. western branch of the Malawi Rift), the map of depth-to-basement shows that the hanging wall of the BMF exhibits a much wider and deeper zone of subsidence in the northern and central sections than in the south (Fig. 5b). The zone of transition between both regions is marked by a shallowly buried pre-rift basement. This shallowly buried basement also coincides with the footwall of the Bwanje Fault, an antithetic fault within the hanging wall of the BMF (see Fig. 2a). Overall, we interpret this 'top-basement' topography to represent a partitioning of depocenters along the BMF hanging wall in which the depocenters in the northern/central sections were once separated from those in the south by a basement-high area. This basement-high has not been significantly buried since the coalescence of the northern/central and southern depocenters. This interpretation is supported (or at least not contradicted) by the relatively shallow basement and distinct hanging wall electrical stratigraphy of ERT Profile 3 (acquired near the transition zone) which contrasts those of the other profiles.

5.2 Evolution of Segmentation and Linkage along the Bilila-Mtakataka Fault

The along-fault distribution of cumulative throw provides insight into how tectonic processes might have contributed to the present-day architecture of normal faults. Our results show the BMF is characterized by a series of relay zones (defined by throw minima) among which the most prominent are those located between the three composite segments (Fig. 6). The lateral continuity of fault

scarp (Fig. 2a) as well as the continuity of offset along the entire fault (Fig. 6) indicate that the relay zones have been breached and that the composite segments are hard-linked. However, among the two major relay zones, the relay zone connecting the Central and Southern composite segments (Kasinje-Chitsulo relay zone in Fig. 4) has the least cumulative throw (Fig, 6), suggesting that it has not accommodated significant long-term tectonic strain post-linkage of the composite segments. Furthermore, the local hanging wall electrical stratigraphy at this relay zone (ERT Profile 3; Figs. 9a-b) shows the presence of discrete resistive bodies, interpreted to be large colluvial deposits of basement boulders dispersed within a mountain front alluvial fan stratigraphy (Fig. 2d). The absence of this unique electrical stratigraphy in the other ERT profiles suggests that this relay zone is, perhaps, a major long-lived entry point for alluvial and colluvial sediments sourced from the BMF footwall into the Makanjira Trough sub-basin.

Based on these observations, and the collocation of this relay zone with the zone of transition between the northern/central and southern BMF depocenters, we infer that the Central-to-Southern composite segment relay zone is likely the most recently breached relay zone along the BMF. It is possible that after the nucleation of the three composite BMF segments, the northern and central composite segments linked first and continued to localize strain which facilitated the early coalescence of their depocenters. It is also likely that progressive offset on the antithetic faults within the BMF hanging wall (e.g., Bwanje Fault) further amplified the subsidence and broadening of the northern and central BMF depocenters (Fig. 5b). In addition, the results of our study suggest that the Southern Composite Segment has accommodated the least cumulative offset and thus, long-term tectonic strain relative to the other composite segments along the BMF. Thus, we interpret that the BMF segments have been accruing vertical offset over the fault life so far, a portion of the long-term faulting activity has been dominated by the breaching of relay zones and linkage of the fault segments leading to the large-scale lengthening of the BMF.

5.3 Implications for Strain Localization During Early-Stage Rifting and Associated Earthquake Hazards

Various studies have investigated the magnitudes of cumulative displacement that a border fault may accommodate before it becomes mechanically incapable of accommodating more strain (Muirhead et al., 2016, 2019; Corti, 2009; Ebinger, 2005; Goldsworthy & Jackson, 2001; Scholz & Contreras, 1998). During this period, the border faults accrue throws greater than 1 km and induce extension within its hanging wall, which is then accommodated by the localization of intra-rift faults as slip rates of border faults progressively reduces (Muirhead et al., 2016). However, it has been shown that pre-existing structures may localize tectonic strain along the rift axis during the early stages of rifting prior to significant displacement accrual on the border faults (Wedmore et al., 2020; Kolawole et al., 2021a). The Malawi Rift has been proposed to have propagated southwards (e.g., Scholz et al., 2020); which implies that the

border faults in the south (such as the BMF) may be relatively less developed than those in the northern sections of the rift, and that a comparison of the long-term displacement on the northern and central Malawi Rift faults with the BMF may provide a template for understanding the future growth of the BMF.

In the northern Malawi Rift (Fig. 1b), where the intra-rift faults account for a significant portion of the overall tectonic strain, the 170 km-long Livingstone border fault records significant displacement (~7.4 km maximum displacement; Fig. 11) (Shillington et al., 2020). Also, the 140 km-long Usisya border fault and the 162 km-long South Basin Border Fault (SBBF) record maximum displacements of ~7.3 km and ~3.85 km respectively in the central and southern parts of Lake Malawi along the rift (Figs. 1b, 11). It is possible that these faults may have reached their maximum displacements and might no longer be accommodating increasing strain as seismic slips (Cowie et al., 2005). Nevertheless, we note that the Livingstone, Usisya, and SBBF have similar fault lengths as the BMF (Fig. 11).

Considering the empirical displacement-length ratio relationships for normal faults (Fig. 11; Kim and Sanderson, 2005; Pan et al., 2020), the BMF should have a similar magnitude of cumulative displacement as the northern and central Malawi border faults, but this is not the case (Fig. 11). Thus, based on the integration of both the subsurface and subaerial components of cumulative fault displacement performed in this study, and a 70 - 75 ° dip (from ERT imaging Figs. 8-10) we estimate the largest cumulative displacement along the BMF to be ~574 m. Thus, we suggest that the BMF is in fact an under-displaced border fault. Furthermore, we posit that this discrepancy in the displacement-length ratio implies that large magnitude seismic activity along the BMF is possible because there is still room for displacement to be accumulated before the border fault potentially becomes inactive as it progressively attains the displacement-length ratio of the larger-offset northern and central Malawi border faults.

Also considering the mathematical expression for the fault displacement-length relationship ($D = CL^n$), the direct proportionality of these two attributes of the fault is dependent on the constant C which could be influenced by factors such as lithology, rheology, strain rate and direction of tectonic stretching, and strain inhibition or transfer to neighboring pre-existing or subsequent structures (Bergen and Shaw, 2010). In the case of the BMF, we speculate that its under-displaced history could be as a result of strain inhibition by and/or distributed transfer of strain to its synthetic Chirobwe-Ntcheu Fault, the southern sections of the SBBF, and the Malombe Fault (prominent border fault along the Malombe Graben (Fig. 1c). In addition, we speculate that Malombe Graben could probably be the more active rift branch and therefore accommodating most of the recent strain and perhaps the Makanjira Trough (and its border fault: BMF) may be dying off.

Furthermore, we estimate strain rates along the BMF as a function of cumulative strain (cumulative displacement) against time (initiation of faulting; 23 Ma (Van Der Beek et al., 1998; Mortimer et al., 2016; Ojo et al., 2021) using the

relationship *strain rate = displacement / time*. The BMF has lower strain rates (0.025 mm/yr) compared to the most prominent and larger offset border faults along the Malawi Rift which include the Livingstone Fault (0.32 mm/yr), Usisya Fault (0.31 mm/yr), and the SBBF (0.20 mm/yr). We suggest that the disparity in displacement may also be due to a combination of lower strain rate of the BMF compared to the Livingstone Fault, Usisya Fault and SBBF, the difference in the normal fault growth model, and to inherited heterogeneities of the crust (Williams et al., 2021 *preprint*).

The presence of potentially recent linkage of composite segments along the BMF indicates a history of prolonged coalescence and offset accrual within the composite segments and a delayed fault lengthening by linkage and coalescence of the composite segments. Thus, we consider a model whereby the BMF could have evolved through alternating stages of lengthening and displacement accrual demonstrating the hybrid fault growth model (Fig. 11; Pan et al., 2020) and/or by fault segment linkage(Peacock, 1991; Peacock and Sanderson, 1991; Cartwright et al., 1988; Peacock et al., 2017).

6.0 Conclusion

We integrated SRTM-DEM, electrical resistivity tomography, and aeromagnetic methods to investigate the architecture and cumulative throw distribution along the Bilila-Mtakataka Fault (BMF). The results show that although the BMF has attained a possible maximum length similar to the other prominent border faults along the northern and central Malawi Rift, it has significantly lower cumulative displacement. We provide evidence suggesting 'recent' linkage and coalescence of the composite segments of the BMF, indicating that much of the fault life has been spent on the coalescence and offset accrual within the composite segments and a delayed fault lengthening by linkage and coalescence of the composite segments. In essence, the BMF is an under-displaced border fault. Our observations highlight the potential for large magnitude seismic activity along the BMF is possible because there is still room for displacement to be accumulated before the border fault potentially becomes inactive and it progressively attains the displacement-length ratio of the larger-offset northern and central Malawi border faults.

In a wider context, the multidisciplinary research approach used in this study is useful for investigating the long-term and short-term structural and tectonic evolution of active normal faults in early-stage continental rift settings as the Malawi Rift. The research approach is especially useful in regions where geological and environmental conditions are unfavorable to the preservation of short-term tectonic indicators (e.g., Rhine Graben and Andean Pre-Cordillera of Western Argentina (Megharoui et al., 2000)).

Acknowledgements and Data

ERT data were collected under the support of NSF II-1358150. Data supporting the conclusions can be found in the cited references and in the supporting information provided as supplements that will also be made available.

Supplementary Information

References

Abbate, E., & Sagri, M. (1980). Volcanites of Ethiopian and Somali Plateaus and major tectonic lines. Atti Convegni Lincei, 47, 219-227.

Bell, R. E., Jackson, C. A.-L., Whipp, P. S., and Clements, B. (2014), Strain migration during multiphase extension: Observations from the northern North Sea, Tectonics, 33, 1936– 1963, doi:10.1002/2014TC003551.

Blakely, R.J., & Simpson, R.W. (1986) Approximating edges of source bodies from magnetic or gravity anomalies, Geophysics, v. 51, p. 1494-1498.

Bonini, M., Corti, G., Innocenti, F., Manetti, P., Mazzarini, F., Abebe, T., and Pecskay, Z. (2005), Evolution of the Main Ethiopian Rift in the frame of Afar and Kenya rifts propagation, Tectonics, 24, TC1007, doi:10.1029/2004TC001680.

Calais, E., d'Oreye, N., Albaric, J. et al. (2008). Strain accommodation by slow slip and dyking in a youthful continental rift, East Africa. Nature 456, 783–787 https://doi.org/10.1038/nature07478

Claerbout, J.F. & Muir, F., 1973. Robust modeling with erratic data, Geophysics, 38(5), 826–844.

Corti, G. (2009). Continental rift evolution: from rift initiation to incipient break-up in the Main Ethiopian Rift, East Africa. Earth-science reviews, 96(1-2), 1-53.

Cowie, P. A., Underhill, J. R., Behn, M. D., Lin, J., & Gill, C. E. (2005). Spatio-temporal evolution of strain accumulation derived from multi-scale observations of Late Jurassic rifting in the northern North Sea: A critical test of models for lithospheric extension. Earth and Planetary Science Letters, 234(3-4), 401-419.

Dawson, A. L., I. K. Kirkpatrick, (1968). The geology of the Cape Maclear peninsula and Lower Bwanje valley, Bull. Geol. Surv. Malaŵi, 71, 71.

deGroot-Hedlin, C. & Constable, S., (1990). Occam's inversion to generate smooth, two dimensional models from magnetotelluric data, Geophysics, 55(12), 1613–1624.

Delvaux, D., 1991. The Karoo to Recent rifting in the western branch of the East-African Rift System: A bibliographical synthesis. Mus. roy. Afr. centr., Tervuren (Belg.), Dépt. Géol. Min., Rapp. ann, 1990(1991), pp.63-83.

Dulanya, Z., Croudace, I., Reed, J.M. and Trauth, M.H., 2014. Palaeolimnological reconstruction of recent environmental change in Lake Malombe (S. Malawi) using multiple proxies. Water SA, 40(4), pp.717-728.

Dulanya, Z., 2017. A review of the geomorphotectonic evolution of the south Malawi rift. Journal of African Earth Sciences, 129, pp.728-738.

Ebinger, C. J., Rosendahl, B. R., & Reynolds, D. J. (1987). Tectonic model of the Malawi rift, Africa. *Tectonophysics*, *141*(1-3), 215-235.

Ebinger, C. J., Deino, A. L., Drake, R. E., & Tesha, A. L. (1989). Chronology of volcanism and rift basin propagation: Rungwe volcanic province, East Africa. Journal of Geophysical Research, 94(B11). https://doi.org/10.1029/jb094ib11p15785

Ebinger, C. (2005). Continental break-up: the East African perspective. Astronomy & Geophysics, 46(2), 2-16.

Ebinger, C., & Scholz, C. A. (2011). Continental rift basins: the East African perspective. Tectonics of sedimentary basins: Recent advances, 183-208.

Ebinger, C.J., Oliva, S.J., Pham, T-Q., Peterson, K., Chindandali, P., Illsley-Kemp, F., Drooff, C., Shillington, D.J., Accardo, N.J., Gallacher, R.J., Gaherty, J., Nyblade, A.A., and Mulibo, G., (2019), Kinematics of Active Deformation in the Malawi Rift and Rungwe Volcanic Province, Africa: Geochemistry, Geophysics, Geosystems, v. 20, p. 3928–3951, https://doi.org/10.1029/2019GC008354.

Faulds, J. E., & Varga, R. J. (1998). The role of accommodation zones and transfer zones in the regional segmentation of extended terranes. Geological Society of America Special Papers, 323, 1-45.

Flannery, J. W., & Rosendahl, B. R. (1990). The seismic stratigraphy of Lake Malawi, Africa: implications for interpreting geological processes in lacustrine rifts. Journal of African Earth Sciences, 10(3), 519–548. https://doi.org/10.1016/0899-5362(90)90104-M

Furman, T., Bryce, J. G., Karson, J., & Iotti, A. (2004). East African Rift System (EARS) plume structure: insights from Quaternary mafic lavas of Turkana, Kenya. Journal of Petrology, 45(5), 1069-1088.

Goldsworthy, M., & Jackson, J. (2001). Migration of activity within normal fault systems: examples from the Quaternary of mainland Greece. Journal of Structural Geology, 23(2-3), 489-506.

Gouiza, M. and Naliboff, J., 2021. Rheological inheritance controls the formation of segmented rifted margins in cratonic lithosphere. Nature communications, 12(1), pp.1-9.

Hodge, M., Fagereng, Å., Biggs, J., & Mdala, H. (2018). Controls on early-rift geometry: New perspectives from the Bilila-Mtakataka Fault, Malawi. *Geophysical Research Letters*, *45*(9), 3896-3905.

Hodge, M., Biggs, J., Fagereng, Å., Elliott, A., Mdala, H., & Mphepo, F. (2019). A semi-automated algorithm to quantify scarp morphology (SPARTA): application to normal faults in southern Malawi. *Solid Earth*, *10*(1), 27-57.

Jackson, J. A., T. Blenkinsop (1993), The Malawi earthquake of March 10, 1989: Deep faulting within the East African rift system, Tectonics, 12, 1131–1139.

Jackson, J., and Blenkinsop, T. (1997), The Bilila-Mtakataka fault in Malawi: An active, 100-km long, normal fault segment in thick seismogenic crust, Tectonics, 16(1), 137– 150, doi:10.1029/96TC02494.

Kim, Y. S., & Sanderson, D. J. (2005). The relationship between displacement and length of faults: a review. Earth-Science Reviews, 68(3-4), 317-334.

Kolawole, F., Phillips, T.B., Atekwana, E.A. and Jackson, C.A.L. (2021a). Structural inheritance controls strain distribution during early continental rifting, rukwa rift. Frontiers in Earth Science, p.670.

Kolawole, F., Firkins, M.C., Al Wahaibi, T.S., Atekwana, E.A. and Soreghan, M.J. (2021b). Rift interaction zones and the stages of rift linkage in active segmented continental rift systems. Basin Research, 33(6), pp.2984-3020.

Laó-Dávila, D. A., Al-Salmi, H. S., Abdelsalam, M. G., & Atekwana, E. A. (2015). Hierarchical segmentation of the Malawi Rift: The influence of inherited lithospheric heterogeneity and kinematics in the evolution of continental rifts. Tectonics, 34(12), 2399–2417. https://doi.org/10.1002/2015TC003953

Loke, M. & Barker, R. (1996). Rapid least-squares inversion of apparent resistivity pseudosections by a quasi-Newton method, Geophys. Prospect., 44(1), 131–152.

Loke, M.H. (2002). Electrical imaging surveys for environmental and engineering studies, A Practical Guide to 2-D and 3-D Surveys: RES2DINV Manual, IRIS Instruments.

Maguire, P. K. H., Ebinger, C. J., Stuart, G. W., Mackenzie, G. D., Whaler, K. A., Kendall, J. M., ... & Harder, S. (2003). Geophysical project in Ethiopia studies continental breakup. EOS, Transactions American Geophysical Union, 84(35), 337-343.

Minsley, B.J., Ball, L.B., Burton, B.L., Caine, J.S., Curry-Elrod, E., and Manning, A.H. (2010). Geophysical characterization of subsurface properties relevant to the hydrology of the Standard Mine in Elk Basin, Colorado, U.S. Geological Survey Open-File Report 2009–1284, p. 7

Morley, C. K., Nelson, R. A., Patton, T. L., & Munn, S. G. (1990). Transfer zones in the East African rift system and their relevance to hydrocarbon exploration in rifts. AAPG bulletin, 74(8), 1234-1253.

Morley, C. K. (1999). Patterns of displacement along large normal faults: implications for basin evolution and fault propagation, based on examples from East Africa. AAPG bulletin, 83(4), 613-634.

Mortimer, E., Kirstein, L. A., Stuart, F. M., & Strecker, M. R. (2016). Spatio-temporal trends in normal-fault segmentation recorded by low-temperature thermochronology: Livingstone fault scarp, Malawi Rift, East African Rift System. Earth and Planetary Science Letters, 455, p. 62–72. https://doi.org/10.1016/j.epsl.2016.08.040

Muirhead, J. D., Kattenhorn, S. A., Lee, H., Mana, S., Turrin, B. D., Fischer, T. P., ... & Stamps, D. S. (2016). Evolution of upper crustal faulting assisted by magmatic volatile release during early-stage continental rift development in the East African Rift. Geosphere, 12(6), 1670-1700.

Muirhead, J. D., Wright, L. J., & Scholz, C. A. (2019). Rift evolution in regions of low magma input in East Africa. Earth and Planetary Science Letters, 506, 332-346.

Nixon, C. W., McNeill, L. C., Bull, J. M., Bell, R. E., Gawthorpe, R. L., Henstock, T. J., ... & Ferentinos, G. (2016). Rapid spatiotemporal variations in rift structure during development of the Corinth Rift, central Greece. Tectonics, 35(5), 1225-1248.

Ojo, O.O., Thomson, S.N. & Laó Dávila, D.A. (2021) - Neogene - Quaternary Rifting of the Southern Malawi Rift and Linkage to the Late Carboniferous – Early Jurassic Shire Rift. (under review at AGU Tectonics)

Palacky, G. (1987) Resistivity Characteristics of Geological Targets. In: Nabighian, M., Ed., Electromagnetic Methods in Applied Geophysics-Theory, Society of Exploration Geophysicists Tulsa, OK, 53-129.

Pan, S., Bell, R. E., Jackson, C. A. L., & Naliboff, J. (2020). Evolution of normal fault displacement and length as continental lithosphere stretches. *Basin Research*.

Roberts, E.M., Stevens, N.J., O'Connor, P.M., Dirks, P.H.G.M., Gottfried, M.D., Clyde, W.C., Armstrong, R.A., Kemp, A.I.S. and Hemming, S., 2012. Initiation of the western branch of the East African Rift coeval with the eastern branch. Nature Geoscience, 5(4), pp.289-294.

Rosendahl, B. R. (1987). Architecture of continental rifts with special reference to East Africa. Annual Review of Earth and Planetary Sciences, 15, 445.

Rotevatn, A., Jackson, C. A. L., Tvedt, A. B., Bell, R. E., & Blækkan, I. (2019). How do normal faults grow?. *Journal of Structural Geology*, *125*, 174-184.

Ryan, W.B.F., S.M. Carbotte, J.O. Coplan, S. O'Hara, A. Melkonian, R. Arko, R.A. Weissel, V. Ferrini, A. Goodwillie, F. Nitsche, J. Bonczkowski, and R. Zemsky (2009), Global Multi-Resolution Topography synthesis, Geochem. Geophys. Geosyst., 10, Q03014, doi:10.1029/2008GC002332.

Shillington, D.J., Scholz, C.A., Chindandali, P.R., Gaherty, J.B., Accardo, N.J., Onyango, E., Ebinger, C.J. and Nyblade, A.A., 2020. Controls on Rift Faulting in the North Basin of the Malawi (Nyasa) Rift, East Africa. Tectonics, 39(3), p.e2019TC005633.

Scholz, C. H., & Contreras, J. C. (1998). Mechanics of continental rift architecture. Geology, 26(11), 967-970.

Specht, T. D., & Rosendahl, B. R. (1989). Architecture of the Lake Malawi Rift, East Africa. Journal of African Earth Sciences, 8(2–4), 355–382.

https://doi.org/10.1016/S0899-5362(89)80032-6

Van der Beek, P., Mbede, E., Andriessen, P., & Delvaux, D. (1998). Denudation history of the Malawi and Rukwa Rift flanks (East African Rift system) from apatite fission track thermochronology. Journal of African Earth Sciences, 26(3), 363–385. https://doi.org/10.1016/S0899-5362(98)00021-9

Walshaw, R.D., 1965. The geology of the Ncheu-Balaka area (No. 19). Government Printer.

Wedmore, L. N., Biggs, J., Williams, J. N., Fagereng, Å., Dulanya, Z., Mphepo, F., & Mdala, H. (2020). Active fault scarps in southern Malawi and their implications for the distribution of strain in incipient continental rifts. Tectonics, 39(3), e2019TC005834.

Williams, J. N., Fagereng, A., Wedmore, L. N., Biggs, J., Mdala, H., Mphepo, F. & Hodge, M. (2021) Low dissipation of earthquake energy along faults that follow pre-existing weaknesses: field and microstructural observations of Malawi's Bilila-Mtakataka Fault, Earth and Space Science Open Archive, DOI = 10.1002/essoar.10507584.1, https://doi.org/10.1002/essoar.10507584.1

Woldegabriel, G., Aronson, J. L., & Walter, R. C. (1990). Geology, geochronology, and rift basin development in the central sector of the Main Ethiopia Rift. Geological Society of America Bulletin, 102(4), 439-458.

WoldeGabriel, G., Olago, D., Dindi, E., & Owor, M. (2016). Genesis of the east African rift system. In Soda Lakes of East Africa (pp. 25-59). Springer, Cham.

Wright, L.J., Muirhead, J.D. and Scholz, C.A., 2020. Spatiotemporal variations in upper crustal extension across the different basement terranes of the Lake Tanganyika Rift, East Africa. Tectonics, 39(3), p.e2019TC006019.

Zanettin, B., EJ, V., & EM, P. (1979). Correlation Among Ethiopian Volcanic Formation with Special Reference to the Chronological and Stratigraphical Problems of the Trap Series.

Zhou, W., Beck, B. F., & Adams, A. L. (2002). Effective electrode array in mapping karst hazards in electrical resistivity tomography. Environmental geology, 42(8), 922-928

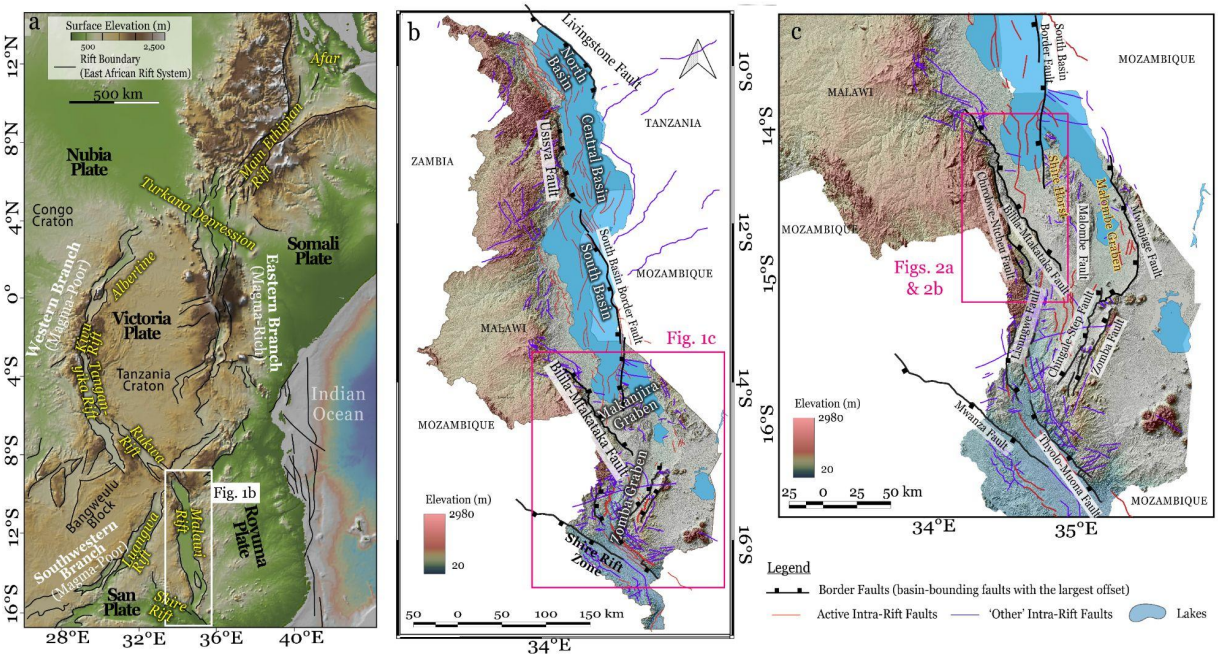

Figure 1: (a) Simplified tectonic map of the East African Rift systems (EARS). Topographic relief basemap is obtained from GeoMapApp (Ryan et al., 2009), (b) Digital elevation model (DEM) hillshade map of the study area highlighting the surface topography, faults, and sub-basins along the Malawi Rift, (c) DEM hillshade map covering the southern Malawi showing structures in both the southern Malawi Rift and the Shire Rift Zone further south. The fault traces are obtained from Malawi Rift's fault database in Williams et al. (2021).

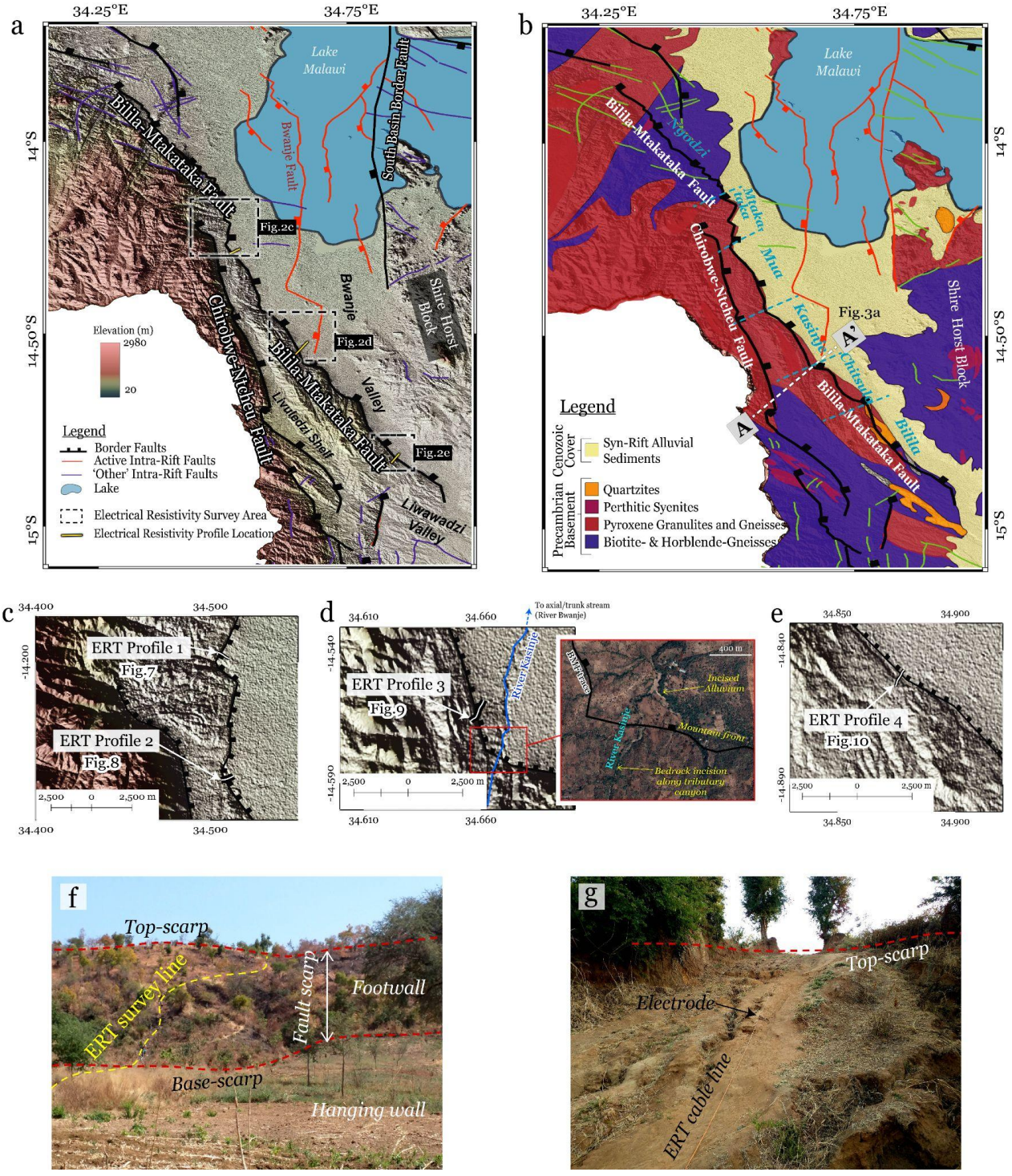
a
34.25°E
34.75°E
14°S
14.50°S
15°S
Lake Malawi
Bilila-Mtakataka Fault
Bwanje Fault
South Basin Border Fault
Fig.2c
Fig.2d
Fig.2e
Bwanje Valley
Shire Horst Block
Chirobwe-Ntcheu Fault
Livulezi Shelf
Liwawadzi Valley
Elevation (m)
2980
20
Legend
Border Faults
Active Intra-Rift Faults
'Other' Intra-Rift Faults
Lake
Electrical Resistivity Survey Area
Electrical Resistivity Profile Location
b
Lake Malawi
Bilila-Mtakataka Fault
Ngodzi
Mtakata Volcs
Mua
Chirobwe-Ntcheu Fault
Kasitu
Chitsulo
Fig.3a
A
A'
Shire Horst Block
Bilila
Legend
Cenozoic Cover
Syn-Rift Alluvial Sediments
Precambrian Basement
Quartzites
Perthitic Syenites
Pyroxene Granulites and Gneisses
Biotite- & Horblende-Gneisses
c
34.400
34.500
-14.200
ERT Profile 1
Fig.7
ERT Profile 2
Fig.8
2,500 0 2,500 m
d
34.610
34.660
-14.540
-14.590
To axial/trunk stream (River Bwanje)
ERT Profile 3
Fig.9
River Kasitu
BMT Fm
400 m
Incised Alluvium
Mountain front
River Kashire
Bedrock incision along tributary canyon
2,500 0 2,500 m
e
34.850
34.900
-14.840
-14.890
ERT Profile 4
Fig.10
2,500 0 2,500 m
f
Top-scarp
ERT survey line
Fault scarp
Footwall
Base-scarp
Hanging wall
g
Top-scarp
Electrode
ERT cable line

Figure 2: (a) Hillshade map of the study area highlighting the surface topography across the Bilila-Mtakataka Fault (BMF) (b) Simplified geologic map of the study area along the BMF showing the major border showing the various lithologic units and BMF and CNF fault traces (BMF – Bilila – Mtakataka Fault; CNF - Chirobwe – Ntcheu Fault) (c)-(e) Electrical resistivity profiles across the BMF; 2c shows the location of electrical resistivity (ERT) Profiles 1 and 2; 2d shows Profile 3, and 2e shows the location of Profile 4. *Figure 2d Inset:* Google Earth© image showing the modern sedimentary geomorphological features in the vicinity of ERT profile 3. (f - g) Field photographs of the deployment and acquisition of ERT profiles across the surface escarpment of the BMF.

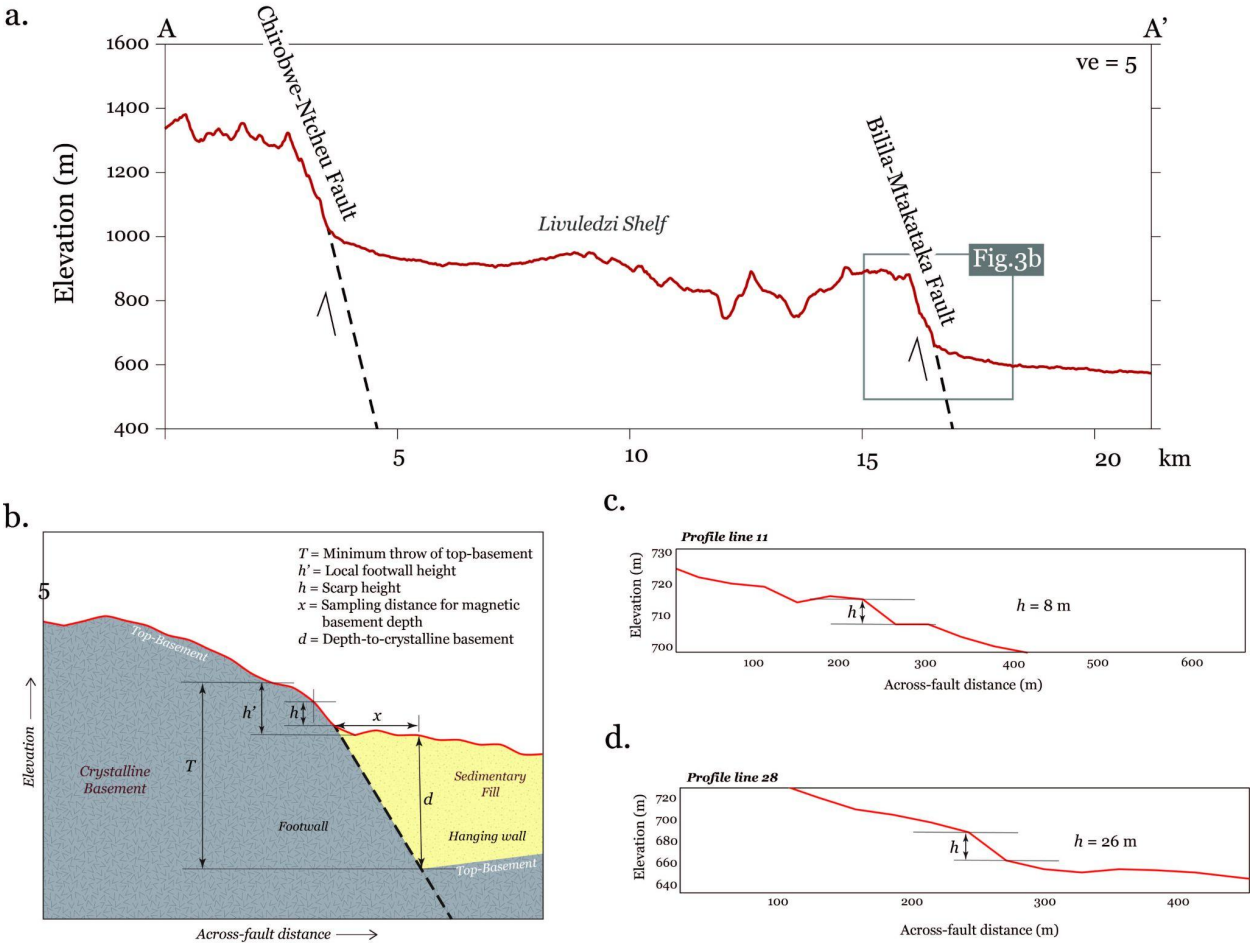

Figure 3: (a) Elevation profile across the Bilila-Mtakataka and the Chirobwe-Ntcheu faults. (b) How the minimum throw (T) was estimated from the measured scarp height (h) and corresponding points of extraction for aeromagnetic depth to magnetic basement (d). (c & d) examples of scarp height measure-

ments.

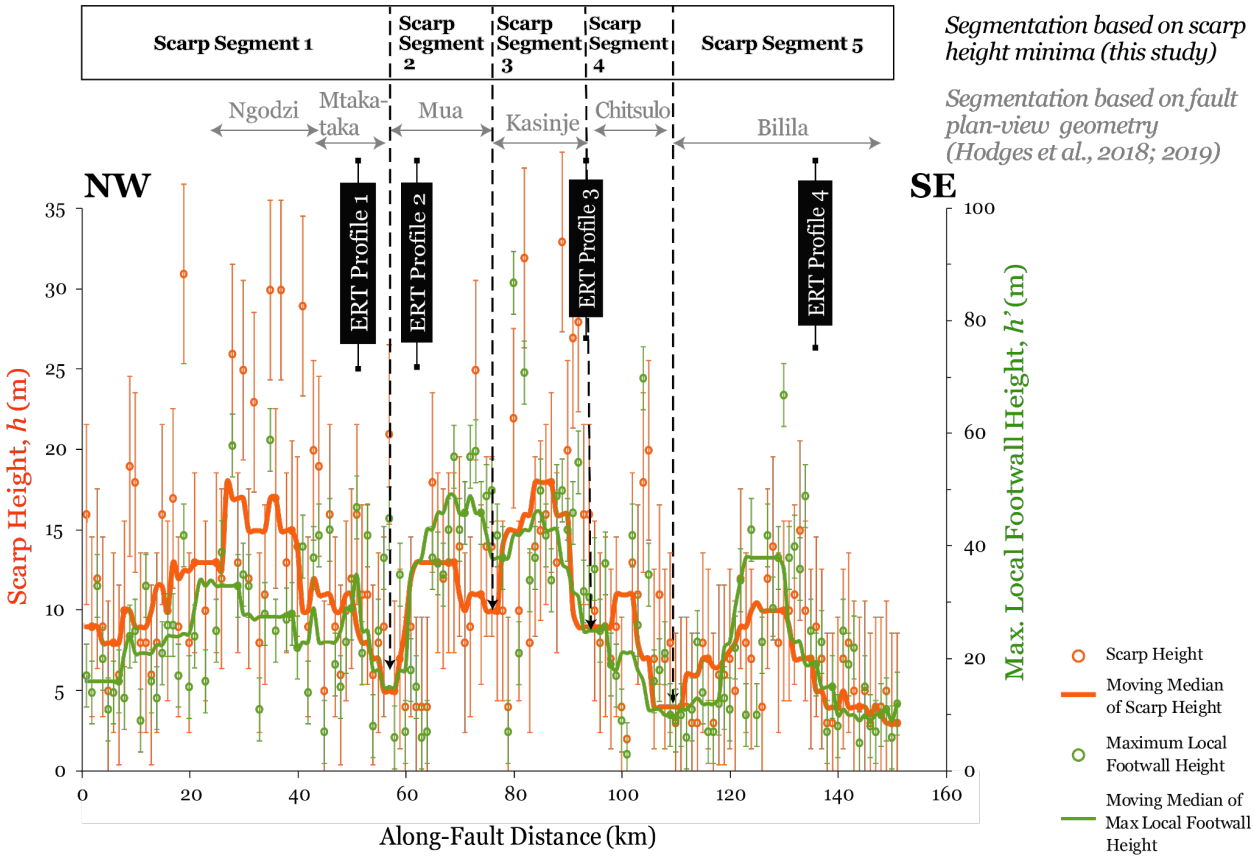

Figure 4: Distribution of scarp height (h) and maximum local footwall elevation (h') versus distance along-strike of the BMF. The 'scarp segments' indicate the fault segmentation based on the scarp height minima along the moving median curve. Segmentation based on plan-view fault geometry is from Hodges et al. (2018). Dashed vertical lines show the location of the locations of the moving median minima which is consistent with the transition from one geometrical segment to another. The error bars show 5.6 m absolute error associated with SRTM-DEM in the vertical directions. Note that the vertical scales are different for scarp height and maximum footwall height plots.

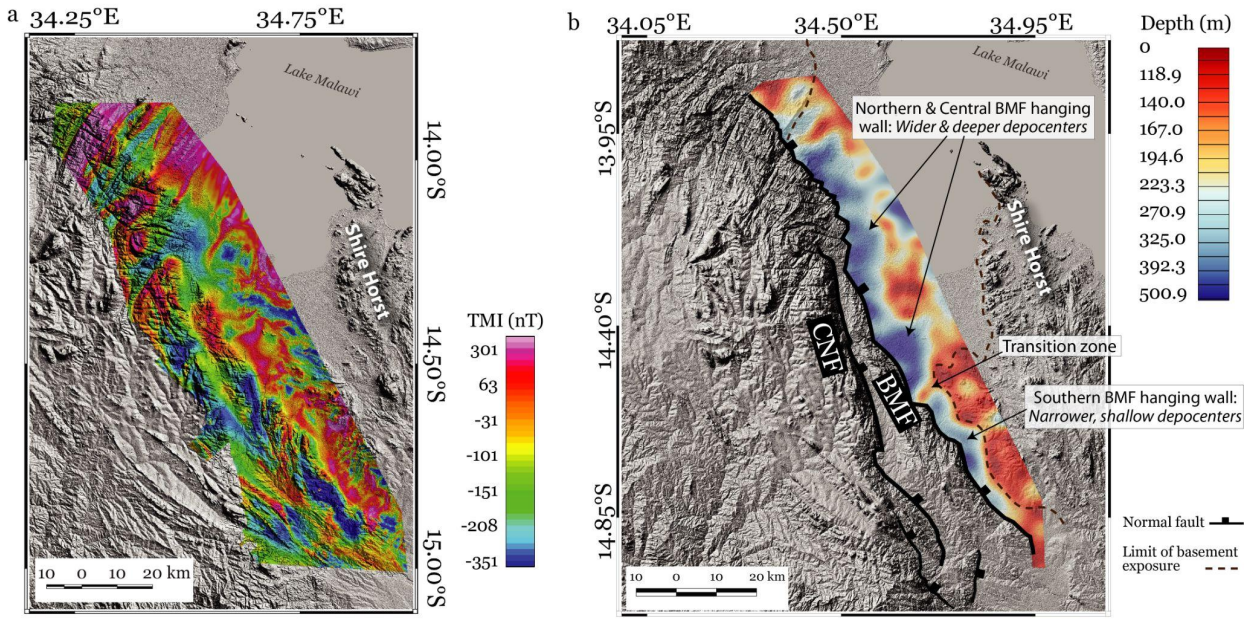

Figure 5: (a) Hillshade map of the study area overlaid with the Total Magnetic Intensity (TMI) aeromagnetic grid, (b) Hillshade map of the study area overlaid with the grid of depth-to-basement solutions estimated from aeromagnetic data, using the Source Parameter Imaging (SPI) technique.

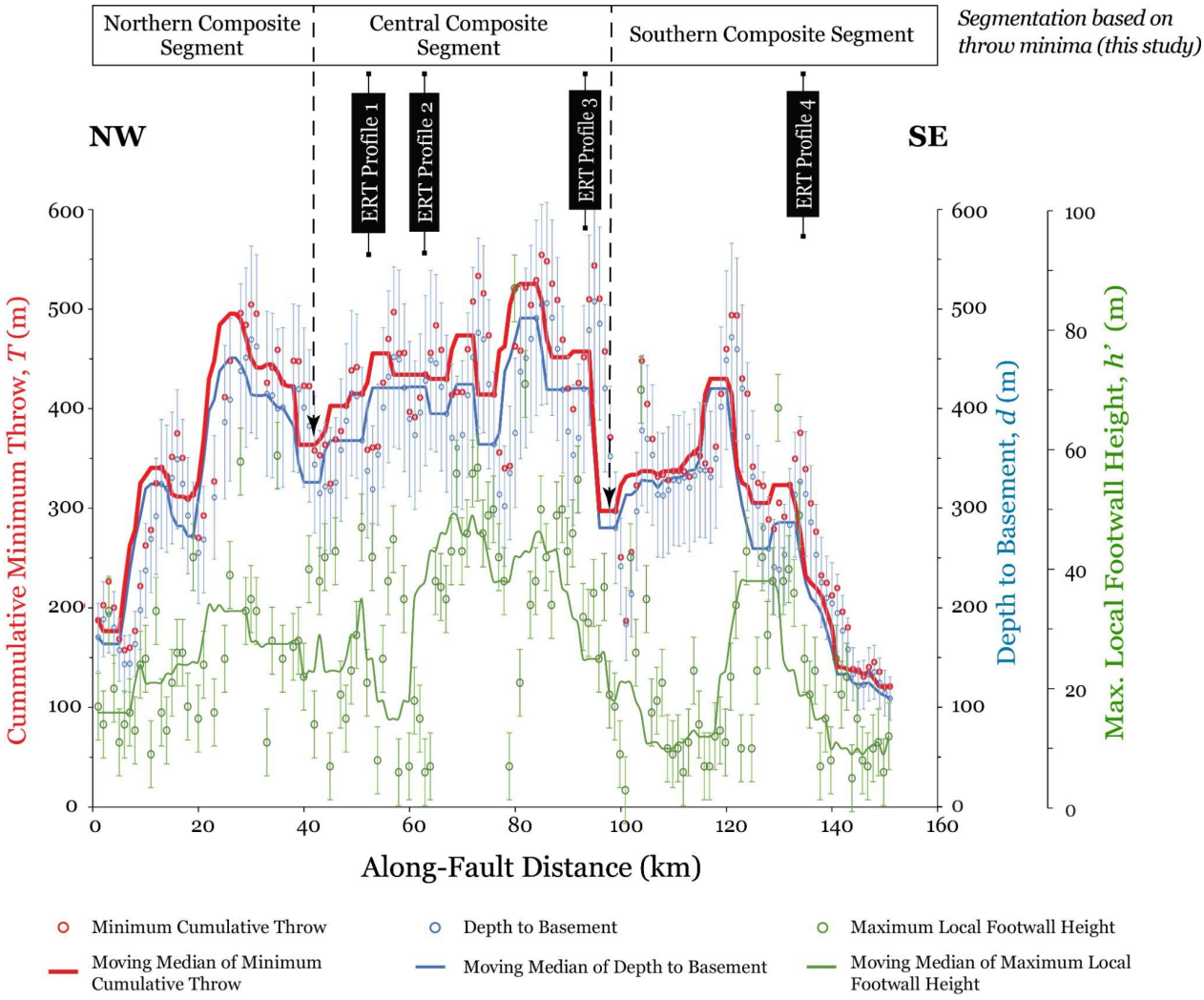

Figure 6: The distribution of cumulative minimum throw estimate based on the addition of depth-to-basement, d and maximum local footwall height, h' at each sampling point along-strike of the fault trace. The error bars on the d data represents ± 20 % accuracy of depth-to-magnetic basement estimates from potential fields data (Gay, 2009), and those on the h' measurements is 5.6 m absolute vertical error of the Shuttle Radar Topography Mission (SRTM) DEM. The dashed lines with arrow-heads indicate the locations of throw minima delineating the large-scale relay zones (i.e. segmentation zones) along the fault.

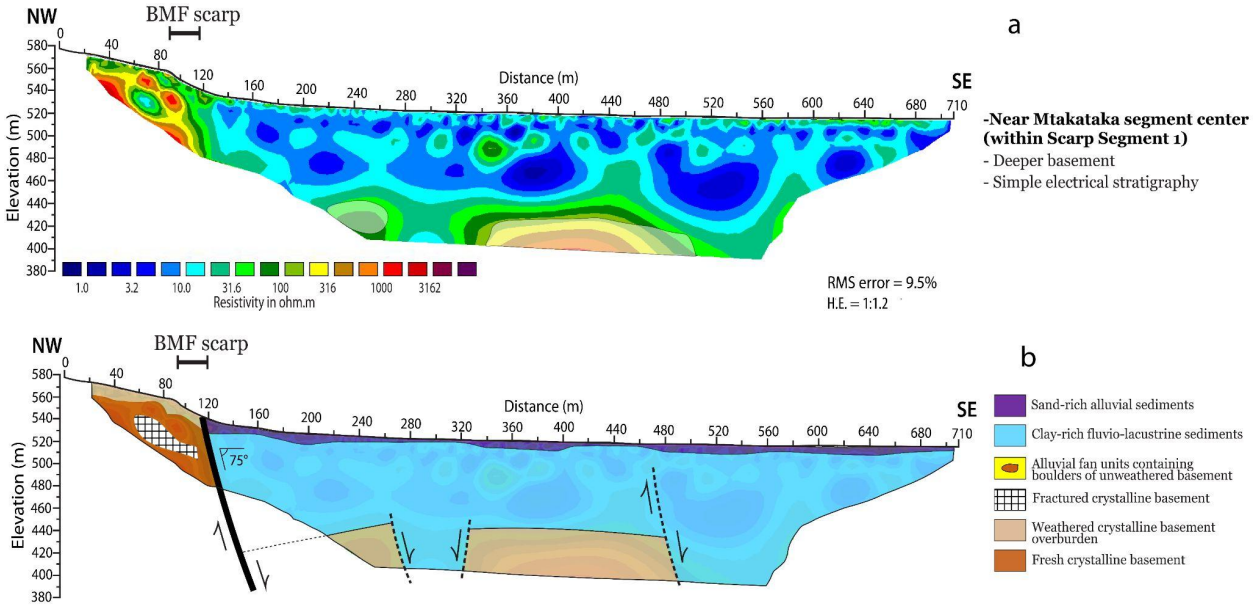

Figure 7: (a) Inverse model of the ERT Profile 1 acquired near the center of Scarp Segment 1 (Ngodzi) in the north-western section of the Bilila-Mtakataka Fault (BMF) (see Fig. 2c). The white transparent polygons are areas of low model sensitivity (see supplementary information figure S1a). (b) Geologic model and interpretation of the resistivity model.

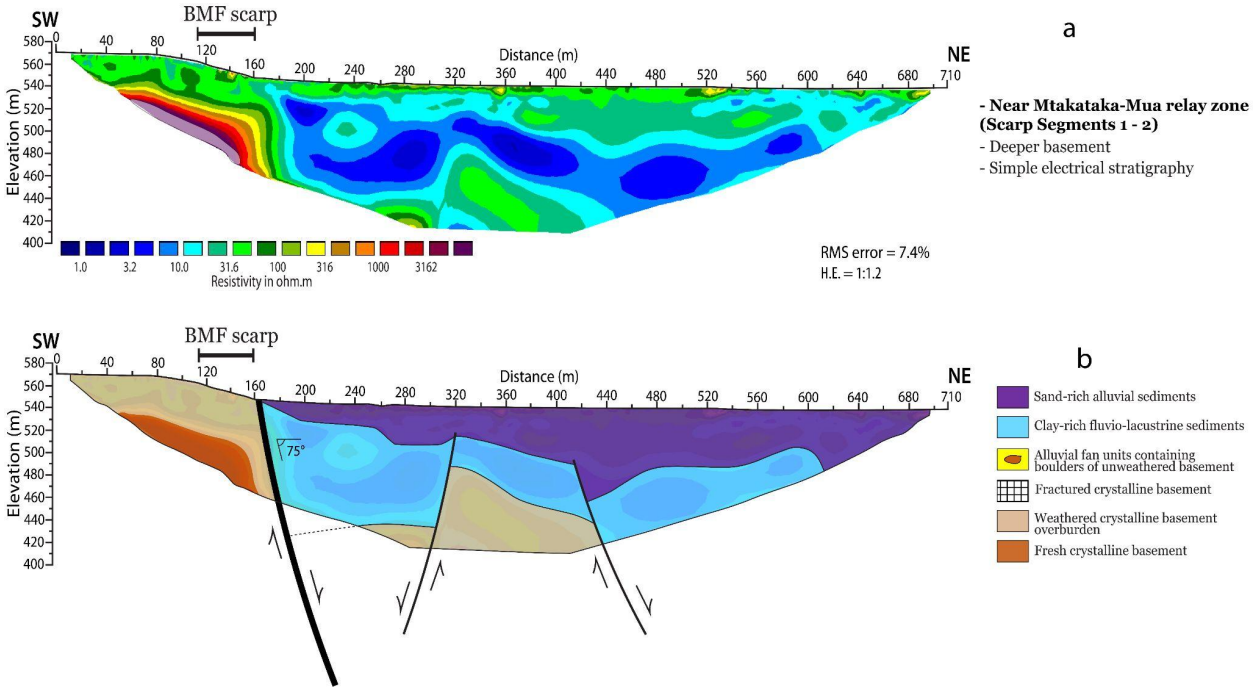

Figure 8: (a) Inverse model of the ERT Profile 2 acquired near the zone of segmentation (relay zone) between Scarp Segments 1 and 2 (transition from Mtakataka to Mua geometrical segments) in the northwestern section of the Bilila-Mtakataka Fault (BMF) (see Fig. 2c). The white transparent polygons are areas of low model sensitivity (see supplementary information figure S1b). (b) Geologic model and interpretation of the resistivity model.

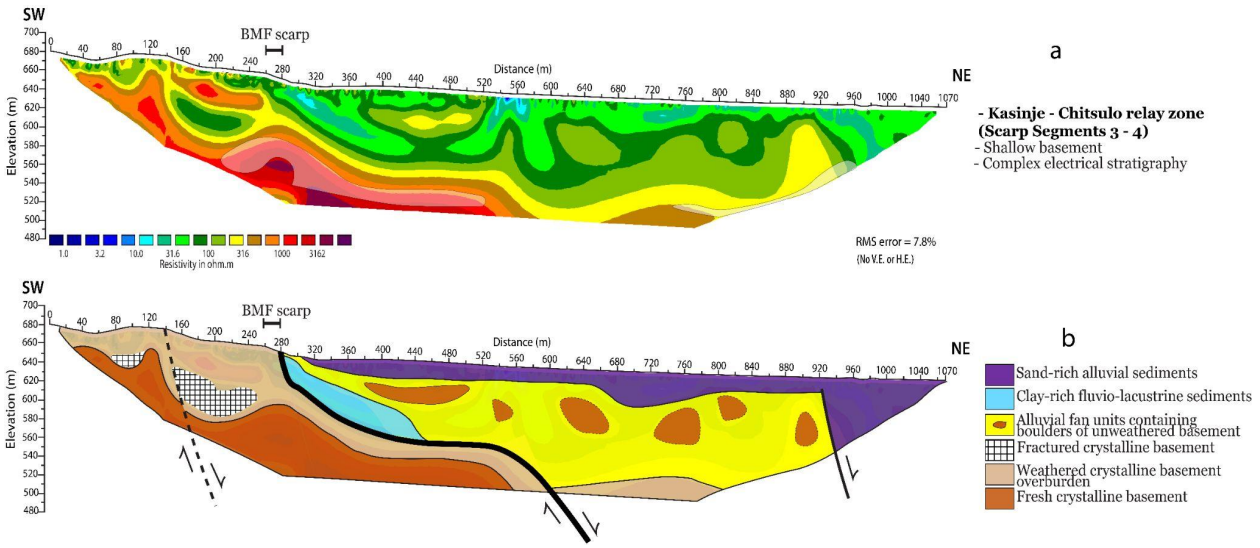

Figure 9: (a) Inverse model of the ERT Profile 3, acquired at the relay zone in-between Scarp Segments 3 and 4 (transition from Kasinje to Citsulo geometrical segments) in the central section of the BMF. The white transparent polygons are areas of low model sensitivity (see supplementary information figure S2a). (b) Geologic model and interpretation of the resistivity model. The inversion model and interpretation reflects a low angle fault plane along the BMF because the survey profile was acquired at an oblique angle to the strike of the fault scarp due to land accessibility challenges encountered on the field.

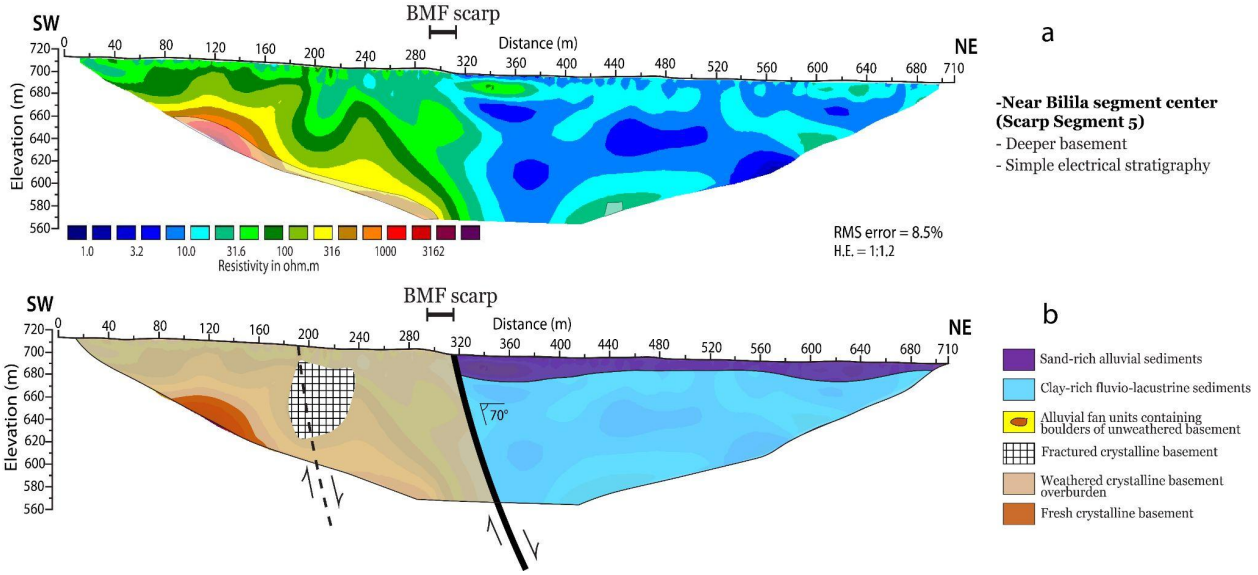

Figure 10: (a) Inverse model of the ERT Profile 4, acquired near the center of the Scarp Segment 5 (Bilila geometrical segment) in the southernmost section of the BMF. The white transparent polygons are areas of low model sensitivity (see supplementary information figure S2b). (b) Geologic model and interpretation of the resistivity model.

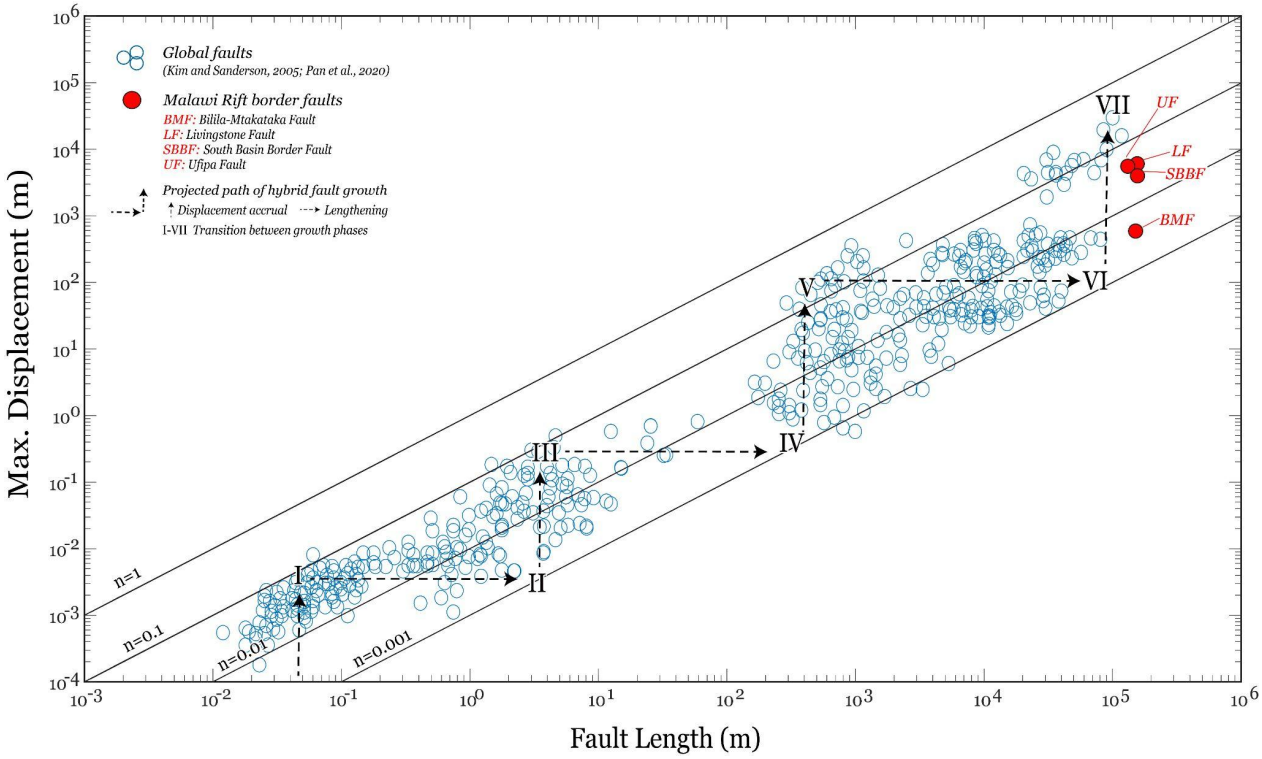

Figure 11: Fault length trace along strike against maximum displacement relationship. The figure shows the stages of strain evolution (I - VII) the Bilila-Mtakataka (BMF) fault is compared with Livingstone Fault (LF) and Usisya Fault (UF) and the tendency for the faults to still accumulate more strain. The arrow lines show the path a fault would follow at different stages (I – VII) as it grows and evolve from initiation to termination (lengthening phase (horizontal arrows); isolated fault initiation and displacement accrual phase (vertical arrows); transition between the normal fault growth phases (I - VI); and at stage VII, fault becomes inactive. The global D-L plots were modified from Kim and Sanderson, (2005) & Pan et al., (2020).